UC Davis
UC Davis Previously Published Works

Title

Non-invasive bladder volume sensing via FMCW radar: Feasibility demonstration in simulated and ex-vivo bladder models

Permalink

Authors

Vafi, Ata
King, Conor
Duan, Hanyi
et al.

Publication Date

DOI

Copyright Information

Peer reviewed

Non-invasive bladder volume sensing via FMCW radar: Feasibility demonstration in simulated and ex-vivo bladder models

Ata Vafi [a,*], Conor King [a], Hanyi Duan [a], Eric A. Kurzrock [b], Soheil Ghiasi [a]

[a] Department of Electrical and Computer Engineering, University of California Davis, Davis, CA, United States
[b] Department of Urology, University of California Davis, Sacramento, CA, United States

ARTICLE INFO

ABSTRACT

This paper presents a proof of concept for noncontact and noninvasive bladder volume sensing in patients suffering from Neurological Lower Urinary Tract Dysfunction (NLUTD) caused by spinal cord injuries. The study investigates the feasibility of utilizing Frequency Modulated Continuous Wave (FMCW) radar as the underlying sensing modality. An algorithm for spectral data analysis is proposed to map radar measurements to bladder volume and is evaluated through MATLAB simulations. Additionally, time domain simulations of a tissue model are conducted to further assess the proposed spectral data analysis algorithm and demonstrate the feasibility of the sensing modality. The effectiveness of the sensing modality is demonstrated through a proof-of-concept measurement setup using an ex-vivo porcine bladder model, which is incrementally filled with saline solution in 200 ml portions. The results of the proposed spectral data analysis on the measured reflected waveforms reveal a strong correlation between the shift in peak frequency and the bladder volume in the model. These findings provide evidence supporting the potential of FMCW radar as a reliable and noninvasive method for continuous bladder volume monitoring.

1. Introduction

Many individuals suffer from the consequences of spinal cord injury (SCI) and congenital spinal anomalies such as spina bifida. In 2016, for example, about 300,000 SCI patients lived in the US (Anon, 2014). Urinary incontinence and a loss of bladder sensation and control are common consequences observed in these patients. In SCI patients, the nerve problems that interfere with signals between the brain and the bladder result in the inability to recognize when their bladder is full and additionally empty the bladder volitionally. This sequela of SCI is termed neurogenic lower urinary tract dysfunction (NLUTD). A chronically overfull bladder with elevated pressure eventually causes detrimental effects such as hydronephrosis, vesicoureteral reflux, urinary tract infections, renal scarring, and ultimately, progression to end stage renal disease (Gormley, 2010; Thorup, Biering-Sorensen, & Cortes, 2012). Most patients with SCI need to empty their bladder every two to four hours with a catheter, termed clean intermittent catheterization (CIC). In CIC, a catheter is inserted through the urethra into the bladder to drain urine on a defined schedule. Since urine is not produced on a regular schedule; SCI patients are recommended to routinely use a catheter every 2 to 4 h during the daytime (4 to 6 times a day). Without timely CIC, patients will leak urine and most need to wear some form of protection, such as an adult diaper. Some patients go so far as to choose a permanent indwelling catheter, which leads to chronic infection and a higher risk of bladder cancer (El-Masri & Fellows, 1981; Nahm, Chen, DeVivo, & Lloyd, 2015; Stonehill William, Dmochowski Roger, Patterson Lynn, &
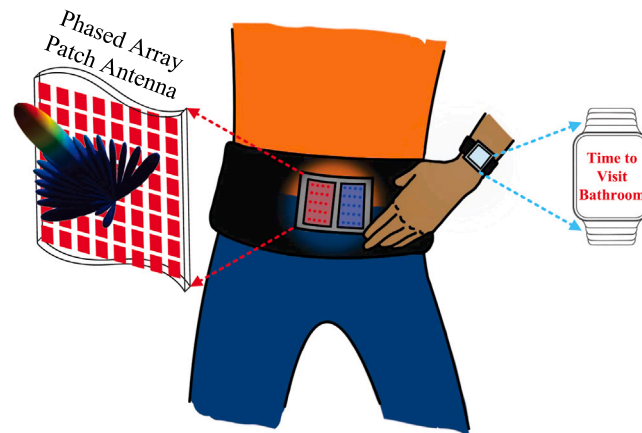
Fig. 1. Conceptual high-level illustration of non-invasive bladder volume detection.

Cox Claire, 1996). Understandably, the inflexible schedule of timely CIC negatively impacts patients' quality of life (QoL), especially considering these patients suffer with mobility difficulty which makes it difficult for them to visit the bathroom. This situation is even worse for quadriplegic patients who depend upon caregivers to perform CIC. The common problem with timed CIC is that during the bathroom visit, patients may only find a small amount of urine in the bladder or they may not get to the bathroom in time and leak urine. Since in reality, it is the bladder volume that dictates the need for bladder emptying rather than time, this research tried to replace the current time-triggered catheterization regimen with volume-triggered (demand-based) timely catheterization. In this regard, SCI patients can greatly benefit from an awareness system that frequently monitors the level of urine inside the patients' bladder and let them know when it is the right time for them to empty. Given a timely alert, patients can plan bathroom trips accordingly, improve compliance with the CIC regimen, protect their kidneys, avoid incontinence, increase social activities, and ultimately, improve their QoL.

2. Proposed approach: FMCW radar

Our proposed method is the use of FMCW radar for the non-invasive detection of urine volume in the human bladder. This method has the potential of extending its use as a non-invasive, small wearable device with a patch-like sensing probe that can be worn by SCI patients. Fig. 1 shows a conceptual high-level illustration for the detection of urine volume in the human bladder.[1] The probe consists of several small size patch antennas in the form of a phase array which will be placed in the lower abdomen (pelvic area) of a patient. The radar transceiver and radar signal processor units will sit on top of the sensing probe and embed inside the patient's waist belt which will be powered by the battery. The radar will proactively trigger measurements to strike a balance between sensing frequency and battery life. The reinforcement-learning techniques will also be used to incrementally improve estimation accuracy as the patients use the device; and will automatically personalize the prediction algorithm to better serve the user patient's specific situation. A patient alert mechanism can be implemented in several possible ways. Examples include on the device (e.g., a discreet ringtone or vibration) for device self-sufficiency; shown on the patient's smart devices (e.g., a smartwatch); implemented by a dedicated uninterruptible alarm (e.g., a vibrating wristband that could be turned off only by the device as the bladder volume reduces: mimicking the natural feeling of urge-to-urinate which is relieved only as the bladder is being emptied); or sent to patient's caregivers. The best strategy would depend on the patient preferences and circumstances. This paper discusses the feasibility of FMCW radar as the underlying sensing modality and is organized as follows: Section 3 discusses the existing approaches for bladder volume sensing which is followed by anatomical and pathophysiological considerations. In Section 4, the FMCW radar principle and the concept of multi-reflection in heterogeneous materials are covered. Section 5 covers the bladder volume sensing via FMCW radar and the noise and nonlinearities in the measured signal; and proposes ways to mitigate the noise and to improve the SNR. It further discusses the FMCW radar design parameters and its trade-offs including the choice of the radar bandwidth to address the range resolution requirement of the project. Section 6 shows the experimental results. The MATLAB simulation result of the proposed spectral data analysis in the case of multi-reflection is shown and discussed in this section. In the following, the time domain simulation result using a multi-layer tissue model of the human abdomen is shown. The discussion of the results assesses the feasibility of the proposed sensing modality. The last part of this section shows the measurement results in an ex-vivo porcine bladder model.

---

[1] This paper is an investigation of sensing modality rather than a developed prototype of a wearable device.

3. Background

3.1. Existing approaches for bladder sensing

Several methods have been evaluated for detecting bladder volume in ambulatory settings, including ultrasound, pressure bio-sensor implants, electrical-impedance tomography (EIT), bio-impedance spectroscopy (BIS) and near-infrared spectroscopy (NIRS). Ultrasound is a commonly used non-invasive method for measuring urine volume in clinical settings. However, its use in ambulatory situations is limited due to the bulky and expensive hardware required. Additionally, ultrasound performance is hindered by body movement and the need to adjust to different body shapes. Furthermore, applying gel between the transducer and the skin to couple the probe to the body is necessary. Despite its widespread use in clinical settings, ultrasound has significant limitations for ambulatory applications. Instead of measuring volume, some studies have attempted to measure bladder pressure by developing implanted biosensors on the urinary wall (Coosemans & Puers, 2005; Majerus et al., 2016; Majerus, Garverick, Suster, Fletter, & Damaser, 2012). However, this method is not effective for several reasons. First and foremost, sustained pressure is detrimental to kidneys, and elevated pressure in the bladder should be avoided, rather than relied upon as an alarm-generation metric. Also, pressure increase occurs close to the time of urinary leakage for most SCI patients. In those cases, pressure-triggered alerts would not provide sufficient time for patients to reach the bathroom and use a catheter. Therefore, monitoring pressure is not a viable method to prevent incontinence for most patients with neurogenic bladder. Another non-invasive approach uses EIT to estimate the conductance distribution of the pelvic region using a belt with multiple electrical contacts (Schlebusch, Nienke, Santos, & Leonhardt, 2013). However, this approach has not been successful in practice, mainly due to unreliable skin contacts, noisy signal acquisition, and inaccurate bladder volume estimation across diverse populations. Similarly, BIS is employed in Vafi et al. (2023) to establish a correlation between changes in bio-impedance data and relative changes in bladder volume. Although this approach showed promising results in ex-vivo bladder models, using the proposed method for the human subject requires a thorough study of the other contributors to the BIS measurement and several limitations that need to be explored before expecting a fully functional system. In another non-invasive approach, a group of researchers utilized NIRS with a single light source-detector pair to determine the full versus void states of the bladder (Fong, Alcantar et al., 2018; Fong, Yu et al., 2018; Molavi, Shadgan, Macnab, & Dumont, 2014). Unfortunately, various noise artifacts, such as geometric variations due to breathing and the exact position of the probe, make it impractical to reliably determine different bladder volumes using the reported NIRS setup. The radar-based technique offers non-invasive and non-contact detection, which has generated increasing interest in biomedical applications. Radar is used (Soganci, Gezici, & Arikan, 2009; Zito et al., 2008) for detection of vital signs in humans including monitoring of respiration and heart beating; radar is also used for cancer recognition and identification of diseases (Davis, Van Veen, Hagness, & Kelcz, 2008; Thiel, Hein, Schwarz, Sachs, & Seifert, 2009). In this context, radar-based detection is proposed as a sensing modality for the detection of urine within the human bladder. The distinct dielectric properties of living tissues, including the much larger permittivity of urine compared to surrounding organs and tissues, provide great potential for detecting and identifying organs using radar. Among different radar types, such as FMCW radar, ultra-wideband (UWB) radar, continuous-wave (CW) radar, and pulse radar, FMCW and UWB radars are the top candidates widely used for medical applications. The use of CW radar is limited by the requirement of separate antennas for the receiver and transmitter, as well as the lack of a timing mark. UWB radar, on the other hand, suffers from low signal-to-noise ratio (SNR), which limits its applicability for our detection purposes. In contrast, FMCW radar benefits from frequency-modulated transmitted signals and enables the use of a time reference for measuring the distance of stationary objects. In this method, the presence of urine in the human bladder can be estimated by analyzing the time delay of the reflections.

3.2. Anatomical and pathophysiological considerations

The kidneys filter blood to produce urine. The urine is transported down the ureters by muscular contractions into the bladder. An empty bladder occupies a small volume and is normally situated behind the pubic bone in both male and female subjects Fig. 2. The bottom of the bladder is fixed in place, and is connected to the urethra. As the bladder fills with urine, its volume increases, and its dome and sides expand into the abdominal cavity (Thiel et al., 2009). The bladder is anterior to the uterus and colon. The tissue between the anterior wall of the bladder and abdominal skin, above the pubic bone (where our device's probe would be placed), is about 2–5 cm thick in most adult patients. The bladder wall thickness is small in comparison, approximately 3 mm (Hakenberg, Linne, Manseck, & Wirth, 2000). The bladder naturally stores urine at extremely low pressures (less than 5 cm of water). The muscles of the bladder accommodate the urine by passive relaxation controlled by the autonomic nervous system. In healthy subjects, even at close to full bladder capacity, the pressure remains low despite strong urges to void. This critically-important low pressure allows the kidneys to continue their filtering function. On the contrary, many bladder diseases and neurologic disorders cause high storage pressures if the bladder volume increases past certain thresholds. High bladder pressure is detrimental to upper urinary tracts, and can cause renal failure, and must be avoided. When a neurologically intact patient decides to void, the brain sends a signal to the brain stem that initiates a cascade of nervous signals and reflexes that allow volitional voiding. The bladder contracts and almost simultaneously the bladder neck and urethral sphincter open. This allows voiding to occur at transient higher pressures between 10 and 40 cm water.(left pane of Fig. 3). For most of us, after the decision to void, we are not cognizant of the intricate processes and coordination that must occur. On rare occasion, we appreciate this miracle when someone walks into the bathroom and we purposefully close our sphincter and hope our bladder stops contracting. For the many patients with spinal cord injuries this less-than-appreciated process is very much a central point of their lives.
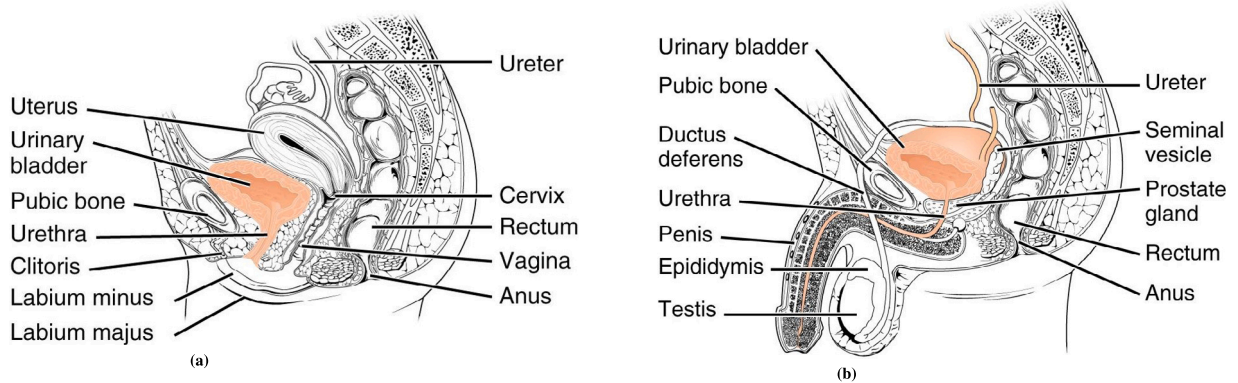
Fig. 2. Urinary bladder **(a)** female subject. **(b)** male subject. Image courtesy of Wikipedia article on Urethra.
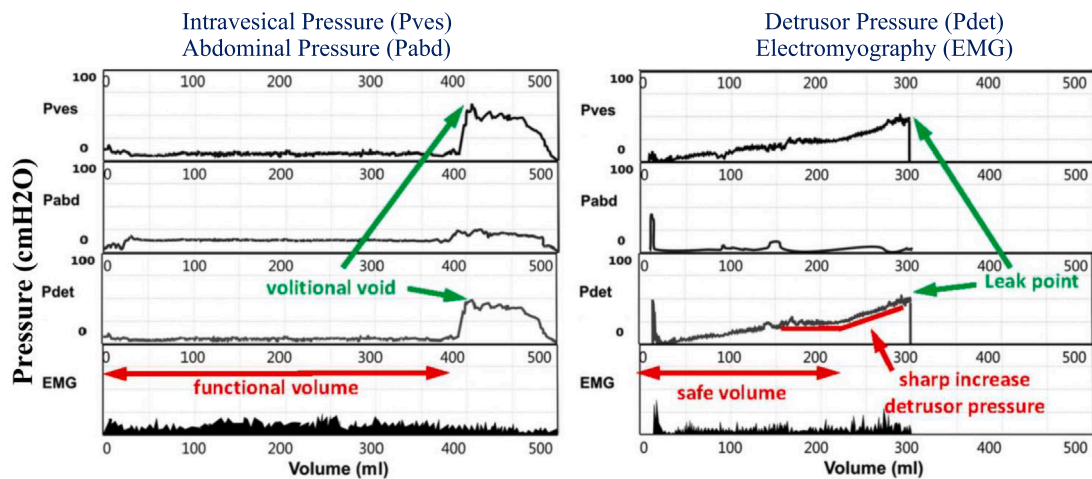

Fig. 3. Representative patterns in urodynamic testing of a healthy female (left) and a 42-year-old male subject with T12 level SCI (right). Pves, Pabd, Pdet, and EMG represent intravesical pressure, abdominal pressure, detrusor pressure, and electromyography, respectively (Hakenberg et al., 2000).

3.3. Urodynamic testing

Urodynamic testing is a clinical test to measure bladder pressure at different fill volumes and to quantitatively characterize the bladder function of a patient. During the test, the patient's bladder is slowly filled with water or contrast media via a dual-lumen urethral catheter, while intravesical pressure (Pves) is simultaneously recorded. Another sensing probe is placed in the rectum to monitor abdominal pressure (Pabd) at the same time. The net pressure due to the bladder wall muscle, detrusor (Pdet), is then derived by subtracting Pabd from Pves shown in Fig. 3. Pressure data channels are plotted against the volume of water instilled by the machine. The patient's bladder has about the same volume as the instilled water by the test machine (small difference due to tubing and such) as long as the patient does not leak. As water is being instilled into the patient's bladder at a constant set rate, e.g., 20 ml per minute, the X axis is also directly proportional to test time. Fig. 3 illustrates an example, in which key patterns of interest to our discussion are highlighted for a healthy subject (left) and a patient with SCI (right). The normal subject (left) shows no significant elevation of bladder wall pressure Pdet (natural bladder stretch to avoid back-pressure on upper urinary tracts) as additional water is instilled into the bladder. When she is asked to void at her capacity, 400 ml for this subject, there is a brisk rise in Pdet due to volitional contraction of her bladder wall muscle. The subject's bladder neck and urethral sphincter open in harmony, and the urine flow out without significant resistance. The volume of instilled water continues to increase in the X-axis of the chart, as the machine continues to run after the patient starts urinating. The patient with T12 level SCI (right pane of Fig. 3) has a slowly rising pressure (demonstrating poor bladder compliance), and then a brisk rise in detrusor pressure starting at a lower volume compared to the healthy subject (200 ml in this example), without any warning or sensation. As the bladder is filled, his detrusor pressure increases until the patient experiences leakage of urine at 300 ml. Such leaks potentially occur at higher detrusor pressure compared to healthy subjects, due to poor coordination between the bladder and sphincter. This SCI patient's safe volume is about 200 ml, and he would be best served by performing CIC before he exceeds his safe volume to avoid risking kidney damage and incontinence (Gormley, 2010; Kurzrock & Polse, 1998). For the sake of brevity, stress leak point pressure and safe pressure
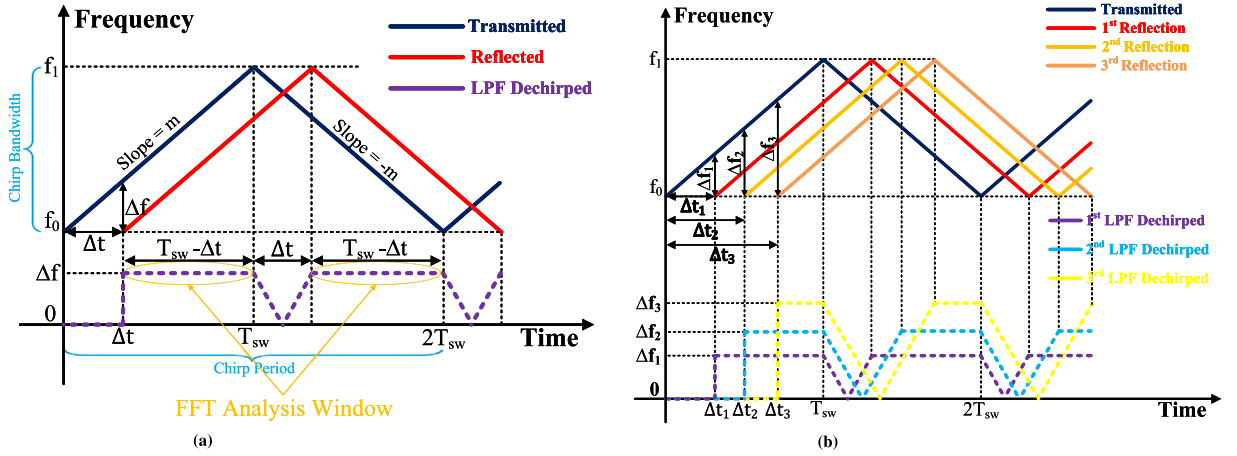
Fig. 4. Instantaneous frequency vs. time for transmitted, received, and LPF dechirped waveforms for triangular chirp signal. **(a)** single-reflection **(b)** multi-reflection.

controversies will not be discussed. SCI patients typically know their safe bladder volume due to repeated CIC and measurements. However, they are unable to sense bladder fullness, and cannot reliably follow a prescribed safe-volume emptying schedule. Our project aims to bridge this gap.

4. FMCW radar as a sensing modality

4.1. Background on FMCW

FMCW radar is a coherent transceiver system that utilizes a chirp waveform as its transmit waveform. The radar's transmitter generates a chirp waveform, which is then transmitted through the transmitting antenna toward a target located at a known distance from the radar. Upon reaching the target, the transmitted waveform interacts with it, causing phase modulation and resulting in a portion of the waveform being reflected back toward the radar. A chirp is a frequency-modulated signal whose instantaneous frequency varies linearly over a fixed period of time (sweep time denoted as T_{sw}) by a modulating signal. Fig. 4(a) illustrates the instantaneous frequency of the transmitted and received triangular chirp waveform for a single target reflection over one period of the chirp. The corresponding mathematical expressions for this waveform are presented in Eqs. (1) and (2). In these equations, $f_{TX}(t)$ and $f_{RX}(t)$ represent the instantaneous frequency of the transmitted and received triangular chirp signals, respectively. Additionally, f_0 denotes the initial frequency at time $t = 0$, f_1 represents the final frequency at time $t = T_{sw}$, and m corresponds to the chirp slope. The chirp slope is a constant value equal to $m = (f_1 - f_0)/T_{sw}$.

$$f_{Tx}(t) = f_1 - m \times |t - T_{sw}| \qquad\qquad 0 \leq t \leq 2 \times T_{sw} \qquad\qquad\qquad (1)$$

$$f_{Rx}(t) = f_{Tx}(t - \Delta t) \qquad\qquad \Delta t \leq t \leq 2 \times T_{sw} + \Delta t \qquad\qquad\qquad (2)$$

Furthermore, the transmitted waveform (denoted as $V_{TX}(t)$) and the reflected waveform (denoted as $V_{RX}(t)$) can be described in the time domain by Eqs. (3) and (4). The received waveform is a scaled and time-delayed version of the transmitted waveform. In Eq. (4), α represents the attenuation factor, which accounts for the impact of path loss and reflection loss. By mixing the received waveform with the transmitted waveform, the instantaneous frequency of the sum and difference between the transmitted and reflected waveforms ($f_{TX}(t) \pm f_{RX}(t)$) are achieved. This processing is known as "dechirping" after which the low-pass component of the output is extracted and further processed to extract the desired information. The instantaneous frequency of the dechirped waveform after passing through a low-pass filter (LPF) is referred to as the beat frequency, as shown in Fig. 4(a) in purple. As observed, the frequency of the LPF dechirped waveform is constant at Δf in certain regions. These regions are referred to as analysis windows, where the waveform can be mathematically expressed using Eq. (5). The waveform spectrum will exhibit a peak at a frequency of Δf and a straight line in its spectrogram.

$$V_{TX}(t) = A_{TX} \times \cos\left(2\pi \int_0^t f_{TX}(t')\,dt'\right) \qquad\qquad 0 \leq t \leq 2 \times T_{sw} \qquad\qquad (3)$$

$$V_{RX}(t) = \alpha \times V_{TX}(t - \Delta t) = A_{RX} \times \cos\left(2\pi \int_{\Delta t}^t f_{TX}(t' - \Delta t)\,dt'\right) \qquad \Delta t \leq t \leq 2 \times T_{sw} + \Delta t \qquad (4)$$

$$V_{IF}(t) = A_{IF} \times \cos(2\pi \times \Delta f \times t + \theta) \qquad where \qquad \theta = 2\pi \int_0^{\Delta t} f_{TX}(t')\,dt' = \omega_0 \times \Delta t + m \times \Delta t^2/2 \qquad 0 \leq t \leq 2 \times T_{sw} \qquad (5)$$

4.2. Electromagnetic interaction with human tissue:

In the case of a heterogeneous material, which can include tissue as well as multiple targets in front of the radar, the reflected waveform will be a superposition of reflections from all the targets and various tissue boundaries. As shown in Fig. 4(b), the time delay between the transmitted and received waveforms gives rise to multiple tones, also known as beat frequencies. Each tone's frequency is proportional to the distance between the transmitter and each boundary of tissue. In this case, the reflected waveform and the LPF dechirped waveform during the analysis windows can be mathematically described using Eqs. (6) and (7), where "n" represents the number of reflections. In the example shown in Fig. 4(b), the reflected waveform consists of three superimposed reflections, resulting in the LPF dechirped waveform having three tones, Δf_1, Δf_2, and Δf_3, during the analysis windows. Consequently, the spectrogram of the waveform displays three straight lines, and the spectrum of the LPF dechirped waveform shows three peaks. A system comprising multiple heterogeneous layers, such as the human abdomen, produces several beat frequencies. However, among these frequencies, only one corresponds to the reflection off the bladder wall, which is the reflection of interest (ROI) due to its correlation with the volume of urine within the bladder.

$$V_{RX}(t) = \sum_{k=1}^{n} A_{RX,k} \times \cos(2\pi \int_{\Delta t_k}^{t} f_{TX}(t' - \Delta t_k) \, dt') \tag{6}$$

$$V_{IF}(t) = \sum_{k=1}^{n} A_{IF,k} \times \cos(2\pi \times \Delta f_k \times t + \theta_k) \tag{7}$$

5. Bladder volume sensing via FMCW radar

In the context of bladder volume sensing using FMCW radar, the radar operates in specific time intervals known as the active mode. Following the active mode, there is a standby mode that lasts for a predetermined period before the radar resumes transmission. During the active mode, the radar detects and processes reflections by dechirping them using the transmitted waveform. Assuming that the only change between consecutive active periods is the reflection associated with changes in urine volume, this correlation can be determined by measuring the amount of shift in the instantaneous frequency of the reflected signal from pre-motion to after-motion. Considering the three reflections illustrated in the case shown in Fig. 4(b), assuming that the last reflection corresponds to the reflection of interest (ROI), specifically representing the position of the bladder wall. Any changes observed in this reflection indicate movement of the bladder wall, which, in turn, reflects variations in urine volume.

This scenario can be expressed using Eqs. (8) and (9), where $V_{RX,Stat}(t)$ denotes the reflections that remain consistent across consecutive active periods. $V_{RX,PM}(t)$ represents the superposition of all reflections during the initial active period (pre-motion), while $V_{RX,AM}(t)$ represents the superposition of all reflections during the subsequent active period (after-motion). The final term in $V_{RX,PM}(t)$ and $V_{RX,AM}(t)$ corresponds to the reflection of interest (ROI), which undergoes changes from pre-motion to after-motion.

$$V_{RX,PM}(t) = \underbrace{\sum_{k=1}^{2} A_{RX,k} \times \cos(2\pi \int_{\Delta t_k}^{t} f_{TX}(t' - \Delta t_k) \, dt')}_{V_{RX,Stat}(t)} + \underbrace{A_{RX3a} \times \cos(2\pi \int_{\Delta t_{3a}}^{t} f_{TX}(t' - \Delta t_{3a}) \, dt')}_{V_{RX,PM-ROI}(t)} \tag{8}$$

$$V_{RX,AM}(t) = \underbrace{\sum_{k=1}^{2} A_{RX,k} \times \cos(2\pi \int_{\Delta t_k}^{t} f_{TX}(t' - \Delta t_k) \, dt')}_{V_{RX,Stat}(t)} + \underbrace{A_{RX3b} \times \cos(2\pi \int_{\Delta t_{3b}}^{t} f_{TX}(t' - \Delta t_{3b}) \, dt')}_{V_{RX,AM-ROI}(t)} \tag{9}$$

Similarly, the resulting LPF dechirped waveform in this scenario can be described using Eqs. (10) and (11). Here, $V_{IF,Stat}(t)$ represents the LPF dechirped waveforms that remain consistent across consecutive radar active periods, $V_{IF,PM}(t)$ represents the superposition of all LPF dechirped waveforms during pre-motion, and $V_{IF,AM}(t)$ represents the superposition of all LPF dechirped waveforms during after-motion. The final term in $V_{IF,PM}(t)$ and $V_{IF,AM}(t)$ corresponds to the LPF dechirped waveform of interest, which undergoes changes from pre-motion to after-motion. To assess the relative changes between these two states, it is necessary to extract $\Delta f_{3a} - \Delta f_{3b}$. Consequently, the spectrum peaks of the LPF dechirped waveforms during pre-motion and after-motion are identified and analyzed.

$$V_{IF,PM}(t) = \underbrace{\sum_{k=1}^{2} A_{IF,k} \times \cos(2\pi \times \Delta f_k \times t + \theta_k)}_{V_{IF,Stat}(t)} + \underbrace{A_{IF,3a} \times \cos(2\pi \times \Delta f_{3a} \times t + \theta_{3a})}_{V_{IF,PM-ROI}(t)} \tag{10}$$

$$V_{IF,AM}(t) = \underbrace{\sum_{k=1}^{2} A_{IF,k} \times \cos(2\pi \times \Delta f_k \times t + \theta_k)}_{V_{IF,Stat}(t)} + \underbrace{A_{IF,3b} \times \cos(2\pi \times \Delta f_{3b} \times t + \theta_{3b})}_{V_{IF,AM-ROI}(t)} \tag{11}$$

5.1. Mitigating non-idealities for SNR improvement

Considering the experimental measurement, it is anticipated that the received waveform will exhibit noise and distortion in both its amplitude and phase. The presence of amplitude noise has a direct impact on the signal-to-noise ratio (SNR) of the receiver. In

other words, the disparity between the signal power and the noise power should be significant enough for the receiver to detect the signal. If this difference is not substantial, the signal will be overwhelmed by the noise floor of the receiver, rendering it undetectable. To enhance the SNR of the received signal, coherent averaging or time-domain averaging techniques can be employed during each active mode of the radar. This can be achieved by dividing the data acquisition time of each active mode into smaller time intervals and capturing multiple LPF dechirped waveforms within each interval. By summing up several LPF dechirped waveforms obtained from different sweeps, the uncorrelated noise can be effectively eliminated, leading to an improvement in the SNR. Assuming that the single reflection during one active period of the radar is corrupted by additive white Gaussian noise (WGN) with a zero mean and a standard deviation of σ, the mathematical expression for the LPF dechirped waveform is given by Eq. (12). In this case, the noise power is σ^2, while the signal power is $A^2/2$. Consequently, the SNR is defined as the ratio of signal power to noise power, which equals $A^2/2\sigma^2$. To improve the SNR, N LPF dechirped waveforms are captured during each active period of the radar and coherently averaged. The resulting waveform can be represented by Eq. (13). In this case, the noise power becomes $N\sigma^2$, while the signal power becomes $(NA)^2/2$. As a result, the SNR achieved using the coherent integrator will be $N \times A^2/2\sigma^2$, indicating an N-fold improvement in the SNR.

$$V_{IF}(t) = A\cos(2\pi \times \Delta f \times t + \theta) + W \qquad W \sim N(0, \sigma) \tag{12}$$

$$V_{IF}(t) = NA\cos(2\pi \times \Delta f \times t + \theta) + \sum_{k=1}^{N} W[k] \tag{13}$$

The presence of noise added to the phase of a signal can have an impact on the positions of peaks within its spectrum. As mentioned earlier, in FMCW radar, the valuable information is encoded in the locations of peaks within the spectrum of the LPF dechirped waveform. Therefore, the accuracy of detection heavily depends on the phase noise and distortion. Assuming that the ideal transmitted waveform described in Eq. (3) is subject to phase noise, the transmitted waveform can be expressed using Eq. (14), where $\phi(t)$ represents the random fluctuations of the transmitted waveform. Since the received waveform is a time-delayed replica of the transmitted waveform, the phase noise of the transmitted waveform will experience the same delay and manifest at the input of the radar receiver. The received waveform can be represented as shown in Eq. (15). Furthermore, Eq. (16) depicts the LPF dechirped waveform, where $\Delta\Phi(t)$ denotes the residual phase noise.

$$V_{TX}(t) = A_{TX} \times \cos(2\pi \int_0^t f_{TX}(t')\, dt' + \phi(t)) \tag{14}$$

$$V_{RX}(t) = \alpha V_{TX}(t - \Delta t) = A_{RX} \times \cos(2\pi \int_{\Delta t}^t f_{TX}(t' - \Delta t)\, dt' + \phi(t - \Delta t)) \tag{15}$$

$$V_{IF} = A_{IF} \times \cos(2\pi \times \Delta f \times t + \theta + \Delta\phi(t)) \qquad where \qquad \Delta\Phi(t) = \Phi(t) - \Phi(t - \Delta t) \tag{16}$$

The noise power spectral density (PSD) of LPF dechirped waveform at an offset frequency of f_0 is expressed in Eq. (17) where $S_\Phi(f_0)$ is the noise PSD of the transmitted waveform. Since the term Δt is usually small for short-range detection, the small-angle approximation is valid and Eq. (17) can be approximated. From Eq. (17) it can be seen that the noise PSD of LPF dechirped waveform increases in proportion to the square of the Δt and the square of the offset frequency. Given a small Δt in the order of nanoseconds, it is expected that the noise PSD of LPF dechirped waveform will be attenuated significantly by the Δt^2 term. In other words, for a small Δt, the phase noise of the reflected waveform from the target is strongly correlated with the phase noise of the transmitted waveform and the residual phase $\Delta\phi(t)$ in Eq. (16) will be negligible and can be ignored. It is expected that for short-range detection, the radar system is not affected by the phase noise of the transmitter.

$$S_{\Delta\Phi}(f_0) = S_\Phi(f_0)\left\{4sin^2(\pi \times \Delta t \times f_0)\right\} \approx S_\Phi(f_0)\left\{4\left(\pi \times \Delta t \times f_0\right)^2\right\} \tag{17}$$

5.1.1. Radar clutters suppression

Any reflected signal from the environment that can be mistaken for the detection of a true target in the radar system is known as clutter. Since any transmitted waveform will generate some amount of sidelobes in the auto-correlation, in the presence of environmental clutter, this can lead to an unwanted peak in the spectrum of the dechirped signal. To reduce the impact of clutter, the transmitted waveform can be encoded such that the sidelobes of the auto-correlation signal are suppressed. This results in a cleaner and more accurate representation of the desired signal, and enables the radar system to better distinguish between true targets and environmental clutter, improving overall detection performance and range resolution. One effective method for sidelobe suppression is the use of phase coding with a Barker code. Barker codes are specific binary code sequences that possess low autocorrelation sidelobes. In Barker code, the peak of the autocorrelation function is equal to N, where N represents the Barker code length, which is limited to 13 code elements. The radar-transmitted waveform phase-coded with the Barker code always has sidelobes with an amplitude less than or equal to 1, resulting in a peak-to-sidelobe ratio (PSR) greater than or equal to N. The Barker codes have a sidelobe structure containing the minimum theoretically possible energy, which is uniformly distributed among the sidelobes. The elements and PSR for different Barker code lengths are shown in Table 1. The time duration of the waveform phase-coded with a Barker code is equal to N multiplied by chirp sweep time (NT_{sw}). For example, when using a Barker code with a length of N=13, the waveform is phase-coded with 13 chirps. The phase coding is performed according to the Barker code sequence as shown in Table 1. In the table, the symbol (+) represents a 0° phase, while the symbol (−) represents a phase shift of 180° (Curry, 2004; Taylor, 1994).

Table 1
The known Barker codes.

Barker code length (N)	Barker code sequence	PSR (dB)
3	+ + −	−9.5
4	+ + −+, + + + −	−12
5	+ + + − +	−14
7	+ + + − − + −	−16.9
11	+ + + − − − + − − + −	−20.8
13	+ + + + + − − + + − + − +	−22.3

5.2. Design parameters, KPIs and trade-offs

In the design of an FMCW radar system, important considerations involve selecting specific parameters such as radar sweep bandwidth (BW), chirp rate (m), operating frequency (f_c), and sampling frequency (f_s). These parameters directly affect key performance indicators (KPIs) of the FMCW radar, including radar resolution (ΔR), range ambiguity, and range accuracy. However, when using FMCW radar as a sensing modality for urine level detection, the target being measured remains stationary. As a result, there is no additional frequency shift in the reflected signal caused by the doppler effect. Therefore, the radar design parameters and KPIs associated with velocity are not considered in this particular study.

5.2.1. Sweep bandwidth and range resolution

As depicted in Fig. 4(a), the chirp bandwidth, denoted as BW, represents the range between the maximum and minimum frequencies covered by the sweeping chirp waveform ($f_1 - f_0$) after it is upconverted. When considering the chirp generated at the baseband, which is centered around 0 frequency, its bandwidth is half of the upconverted waveform's bandwidth. This is due to the definition of bandwidth as the positive part of the spectrum, while half of the spectra of any baseband waveform are negative. Similarly, the chirp slope, denoted as m, is defined for the upconverted transmitted waveform and is equal to $m = BW/T_{sw}$, where T_{sw} represents the sweep time. To ensure the radar system meets the required range resolution (ΔR) and depth specifications, it is necessary to determine the chirp bandwidth and sweep period. Range resolution refers to the radar's ability to distinguish between closely spaced objects. When two closely spaced objects have similar chirp slopes and propagation speeds, the range resolution can be calculated using the expression ($\Delta R = v_p(\Delta f - \Delta f')/(2 \times m)$) as an extension of Eq. (19). In this equation, $\Delta f - \Delta f'$ represents the beat frequency difference between the closely spaced objects, which is limited by the FFT resolution. The FFT resolution corresponds to a one bin difference in the FFT and is equal to f_s/N_s for real-valued signals due to Hermitian symmetry. Here, f_s denotes the sampling frequency of the LPF dechirped waveform, and N_s is the total number of samples acquired during the data acquisition time denoted as T. Considering that the rate at which the samples are acquired divided by the number of samples is the inverse of the acquisition window (1/T), $\Delta f - \Delta f' = f_s/N_s = 1/T$ results. Simplifying the equation for ΔR, we obtain $\Delta R = v_p/(2 \times m \times T)$. By substituting the expression for m as $m = BW/T_{sw}$, the equation for range resolution in FMCW radar using a triangular chirp further simplifies to Eq. (18).

$$\Delta R = \frac{V_p}{2 \times m \times T} = \frac{V_p \times T_{sw}}{2 \times BW \times T} \tag{18}$$

As depicted in Eq. (18), the range resolution is directly proportional to v_p and T_{sw}, while it is inversely proportional to the chirp bandwidth and data acquisition time. The higher bandwidth the chirp sweeps, the better range resolution will be achieved ($BW \uparrow \Rightarrow \Delta R \downarrow$).

5.2.2. Radar operating frequency

The selection of the radar operating frequency band is crucial to meet the desired penetration depth requirement. The penetration depth refers to the depth at which an electromagnetic field can effectively penetrate into the body, reaching approximately 37% of its original amplitude. It is influenced by factors such as tissue composition, radiation intensity, and the frequency of operation. Tissue composition, which includes the distribution of ions and water molecules, plays a significant role in the absorption of the electromagnetic field. Tissues with higher water or salt content tend to exhibit greater absorption and a thermal increase, resulting in higher absorption within the tissue. Conversely, tissues with lower water or salt content tend to have a larger penetration depth. The penetration depth is also influenced by the effective radiated power (ERP) of the radar. Higher ERP values generally lead to increased penetration depth. However, it is important to consider the maximum permissible exposure level set by regulations such as those defined by the FCC. These regulations impose limits on the maximum ERP and associated depth to ensure safety during human body exposure to electromagnetic waves. Since tissue composition and ERP are factors beyond the control of radar designers, the selection of operating frequency becomes a critical parameter to control the penetration depth. In general, higher operating frequencies (shorter wavelengths) result in stronger absorption at the body surface and shallower penetration depths. This is due to the fact that tissue conductivity typically increases with frequency, leading to a trade-off between resolution and penetration depth in radar design. At frequencies above 10 GHz, the radiation incident on the human body is predominantly absorbed or reflected by the skin layer. The penetration depth, as illustrated in Fig. 5, varies for different tissue types. This discrepancy is attributed to the tissue's thermal characteristics, which are influenced by variations in water content. Tissues with higher water content exhibit greater absorption, leading to a conversion of field energy into heat rather than deeper penetration. Additionally, Fig. 5 demonstrates
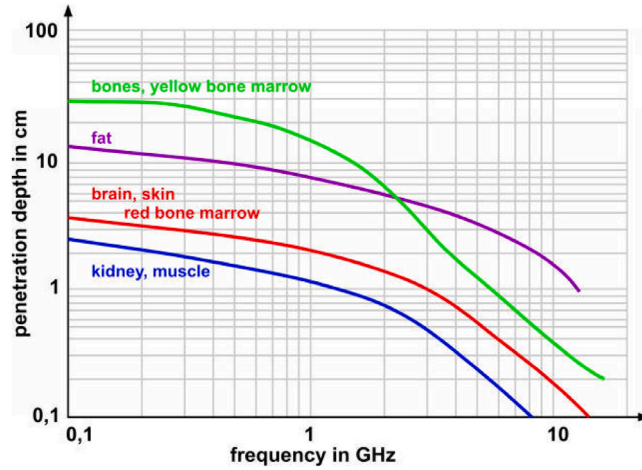
Fig. 5. Penetration depth of EM wave in different body tissues types versus frequency (EMF-Portal, 2023).

that, for a particular tissue type, the penetration depth decreases with increasing field frequency. To determine the appropriate radar operating frequency for our application, a human abdomen model was created using CST Studio Suite, and specific absorption rate (SAR) simulations were conducted. The details of these simulations are discussed in Section 6.4.

5.2.3. Radar sampling frequency (f_s)

According to the Nyquist rate criterion, the radar's sampling frequency should be at least twice the maximum frequency of the LPF dechirped waveform ($f_s = BW$). The maximum beat frequency (Δf_{max}) generated in the baseband can be substituted into Eq. (19) to calculate the maximum range (R_{max}). In this case, $\Delta f_{max} = BW = f_s$. By substituting this expression in Eq. (19), we obtain $R_{max} = (f_s \times v_p)/(2 \times m)$. This equation reveals that for the same required R_{max} and the same chirp bandwidth, a chirp with a lower slope (m↓) requires a smaller ADC sampling frequency, but at the expense of a longer sweep period ($f_s \downarrow => T_{sw} \uparrow$). Conversely, a higher slope (m↑) necessitates a higher ADC sampling frequency while reducing the sweep period ($f_s \uparrow => T_{sw} \downarrow$).

5.2.4. Radar sweep period

The chirp sweep period is selected to meet the requirements for the maximum unambiguous range (R_{max}) that the radar signal can detect. The chirp period is equal to two times of the sweep time for triangular chirp ($T = 2 \times T_{sw}$) and it is selected to be at least 5 to 6 times of round-trip time (Δt) so that the reflected signal from the target is received before a single period of frequency modulation is completed. The round-trip time is the time the transmitted signal travels in space, reaches the target, hits it, and scatters back to the receiver antenna and it is equal to the round-trip distance divided by the propagation speed of the EM wave inside the human body ($\Delta t = 2 \times R_{max}/v_p$). From Fig. 4(a), taking the slope of the frequency deviation function for a single sweep interval, the relation between the beat frequency and range information is obtained, as shown in Eq. (19).

$$m = \frac{BW}{T_{sw}} = \frac{\Delta f}{\Delta t} = \frac{\Delta f}{(2 \times R)/V_p} \rightarrow R = \frac{\Delta f \times V_p}{2 \times m} \qquad (19)$$

From Eq. (19), it is also clear that for a given chirp bandwidth, the lower the sweep period is, the higher the Δf will be, which means better distinction of different reflections.

6. Experimental results

6.1. Multilayer modeling of abdominal tissue

When an electric field is applied to the tissue, a charge displacement in the tissue causes dielectric polarization. This feature enables the biological tissues to be modeled using their dielectric properties. The dielectric properties describe both the frequency-dependent permittivity and conductivity/losses of biological tissues and their interaction with an external electric field. The real and the imaginary terms of the complex permittivity are related by Eq. (20) where $\epsilon'(\omega)$, known as dielectric constant, expresses the amount of energy stored in the tissue when an external electric field is applied and the $\epsilon''(\omega)$ indicates the amount of energy loss from the tissue due to an external electric field. It reflects the dissipative nature of the tissue which absorbs the energy and partially converts it to heat and it is related to the conductivity by $\epsilon''(\omega) = \sigma(\omega)/\omega$.

$$\epsilon(\omega) = \epsilon'(\omega) - i\epsilon''(\omega) = \epsilon'(\omega) - i\frac{\sigma(\omega)}{\omega} \qquad (20)$$
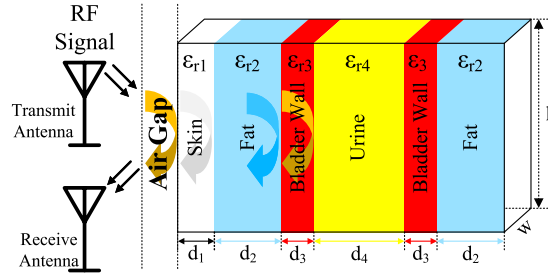
Fig. 6. Multi-reflection in the multilayer tissue model with different permittivity.

The phase velocity, absorption rate and penetration depth of the electromagnetic plane wave inside the tissue depend on the dielectric properties of the tissue which can be expressed by Maxwell's curl equations. As shown in Fig. 6, the human abdomen can be modeled as a multilayer heterogeneous structure. Each of the layers (e.g., skin, fat, etc.) is a tissue with distinct dielectric properties from one to the other. The difference in dielectric properties, causes the reflection to happen at tissue boundaries. Since the value of the relative permittivity of the urine is much larger than the surrounding organs and tissues, it is expected to have a large reflection of the incident EM wave at its boundary. Fig. 6 shows the multi-reflection of EM wave at the boundaries between the various tissues with different permittivity. The received signal is a superposition of reflections from all of the boundaries.

6.2. MATLAB simulation of FMCW

The MATLAB simulation was performed to replicate the real-world scenario of multi-reflection, where the received signal consists of reflections from different organs on its path toward the bladder. Two models were developed in MATLAB: one representing the ideal case and the other incorporating noise affecting the reflected signal. The spectral data analysis was performed for both scenarios. In both models, a simulation of FMCW radar was carried out with three targets located at distances of $R_1 = 9$ m, $R_2 = 26$ m, and $R_3 = 41$ m from the radar. It was expected that the reflected waveform would be a superposition of reflections from each target, resulting in three straight lines in the spectrogram of the LPF dechirped waveform and three peaks in its spectrum. The position of each peak was expected to correlate with the location of each target. For this particular scenario, the radar was set to operate at a frequency of $f_c = 2.5$ GHz, and the chirp was designed to have a sweep bandwidth of 1 GHz over a duration of 1.6 μs, corresponding to a slope of 1250 MHz/μs. Based on the radar parameters, the delay between the transmitted and received signals was expected to be $\Delta t_1 = 60.04$ ns, $\Delta t_2 = 173.45$ ns, and $\Delta t_3 = 273.52$ ns for the respective targets, as calculated using the equation $\Delta t = 2 \times R/v_p$. By applying these calculated delay times in Eq. (19), it was expected that the power spectral density (PSD) of the LPF dechirped waveform would exhibit peaks at $\Delta t_1 = 75.05$ MHz, $\Delta t_2 = 216.82$ MHz, and $\Delta t_3 = 341.9$ MHz, respectively. The radar parameters, target parameters, and corresponding target delays are summarized in Table 2b.

Table 2

(a) FMCW radar ideal model specification.	
Operating frequency (f_c)	2.5 GHz
Sweep period ($2 \times T_{sw}$)	1.6 μs
Sweep bandwidth (BW)	1 GHz
Sample rate (f_s)	2.5 GHz
Range resolution ($\Delta R = v_p/(2 \times BW)$)	15 cm
Chirp slope (m = BW/T_{sw})	1250 MHz/μs
$f_0 = f_c - BW/2$	2.5 GHz
$f_1 = f_c + BW/2$	3.5 GHz

(b) Target parameters.				
Target	1st	2nd	3rd *Pre − Motion*	3rd *After − Motion*
Range [m]	9	2	41	50
TOF [ns]	60.04	173.45	273.52	333.56
Beat Freq [MHz]	75.05	216.82	341.9	416.96

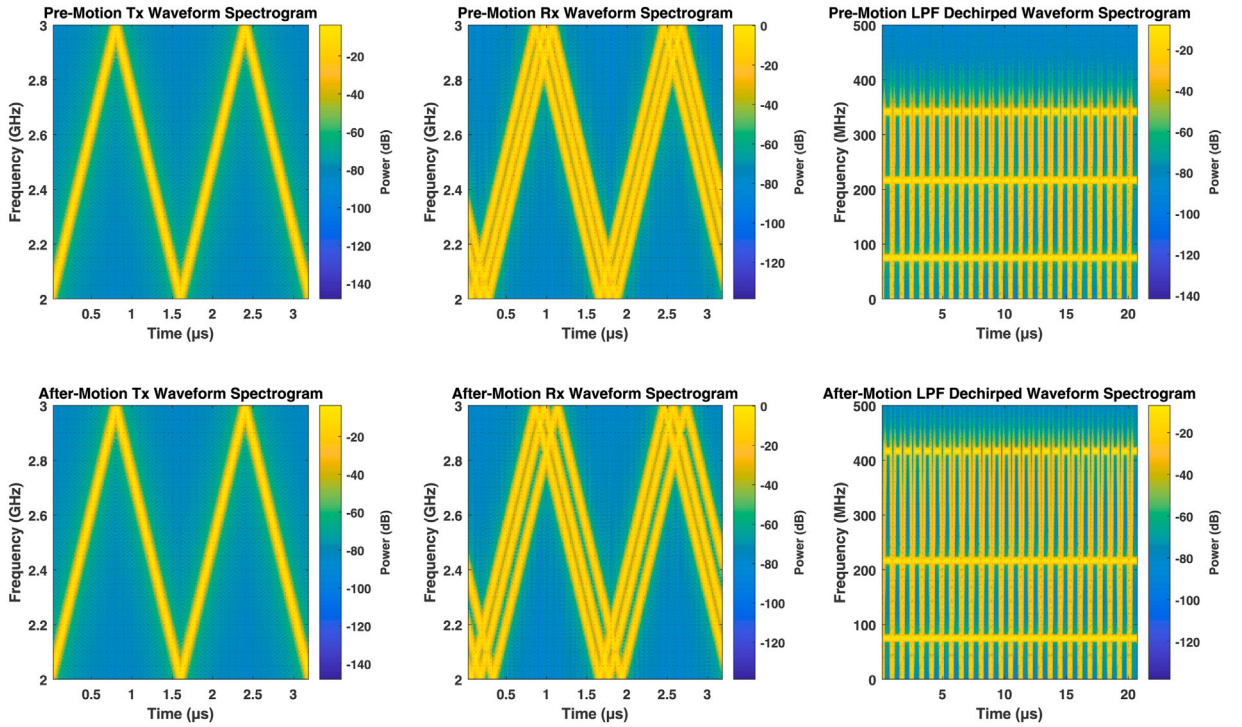| (c) FMCW radar non-ideal model specification.		
Tx Power (P_{TX})	[dBm]	5
Total Tx Gain ($G_{total,TX}$)	[dB]	6.5
$P_{rad|dBm} = P_{TX|dBm} + G_{total,TX|dB}$	[dB]	11.5
Total Rx Gain ($G_{total,RX}$)	[dB]	12.3
Total Channel Loss (A_{Loss})	[dB]	140
Rx Noise Figure (NF)	[dB]	4.5

Fig. 7. Spectrogram of transmitted, received and LPF dechirped waveform: **(Top)** Pre-Motion **(Bottom)** After-Motion. The shift in the PSD 3rd peak from 341.87 MHz to 417.5 MHz due to the change in the 3rd target location from 41 m to 50 m.

The top row of Fig. 7 shows the simulation results for the spectrogram of the transmitted, received, and LPF dechirped waveforms. As can be seen, the transmitted waveform spectrogram is a triangle centered at 2.5 GHz with a sweep of 1 GHz. The received waveform spectrogram is the superposition of three time-delayed copies of the transmitted waveform, resulting in three straight lines in the spectrogram of the LPF dechirped waveforms and three distinct tones in its spectrum. In the left plot of Fig. 8(a), the spectrum of the LPF dechirped waveform shows distinct peaks at the frequencies predicted in Table 2b, demonstrating the successful extraction of target information using this method. The locations of these peaks align with the expected frequencies. Next, an after-motion simulation was performed by changing the position of the third target from 41 m to 50 m, resulting in a new delay of $\Delta t_3 = 333.56$ ns and a new beat frequency of $\Delta t_3 = 416.96$ MHz. The positions of the other targets remained unchanged. The after-motion target parameters are summarized in Table 2b, in the last column under target parameters. The results reveal that the lines in the spectrogram and the peaks in the spectrum corresponding to the first two targets remain the same compared to the previous simulation. However, those representing the third target exhibit changes, as shown in Figs. 7 and 8(b). The difference between the positions of the last peaks in the spectrum before and after the motion, as depicted in the right plot of Fig. 8(b), directly corresponds to the relative change in the position of the third target.

To replicate the nonidealities observed in experimental measurements, WGN is added to the amplitude of the received signals in the MATLAB simulation. The communication channel between the transmitter and receiver is modeled as lossy to account for any signals absorbed by the human body. In this simulation, the transmitter is assumed to have a total gain of 6.5 dB and a transmitted power of 5 dBm, resulting in a total radiated power of 11.5 dB. The communication channel is modeled with a loss of 140 dB at the radar operating frequency. The receiver is assumed to have a total gain of 12.3 dB with a noise figure of 4.5 dB. These parameters are summarized in Table 2c. To improve the SNR of the received signal by reducing uncorrelated noise, a coherent averaging technique is utilized in the MATLAB simulation, as explained in 5.1. In this simulation, 64 LPF dechirped waveforms from different sweeps are added together and averaged. The simulation result of this is shown in Fig. 9(a), where the peaks are observed at the expected locations. To further enhance the simulation, the sidelobes of the transmitting waveform are suppressed using phase coding with a Barker code of length $N = 13$, as explained in 5.1.1. The simulation result utilizing Barker code is shown in Fig. 9(b). As can be observed, the noise in this simulation is significantly reduced compared to the previous simulation, while the positions of the peaks remain the same, demonstrating the effectiveness of this method in SNR improvement.

6.3. Time domain simulation of multi-reflection in multilayer tissue

The multilayer model of the human abdomen shown in Fig. 6 is built in CST Studio Suite; the CST model is shown in Fig. 10. The time domain simulation was performed in CST Studio Suite. The dielectric properties of each tissue were obtained from Gabriel,
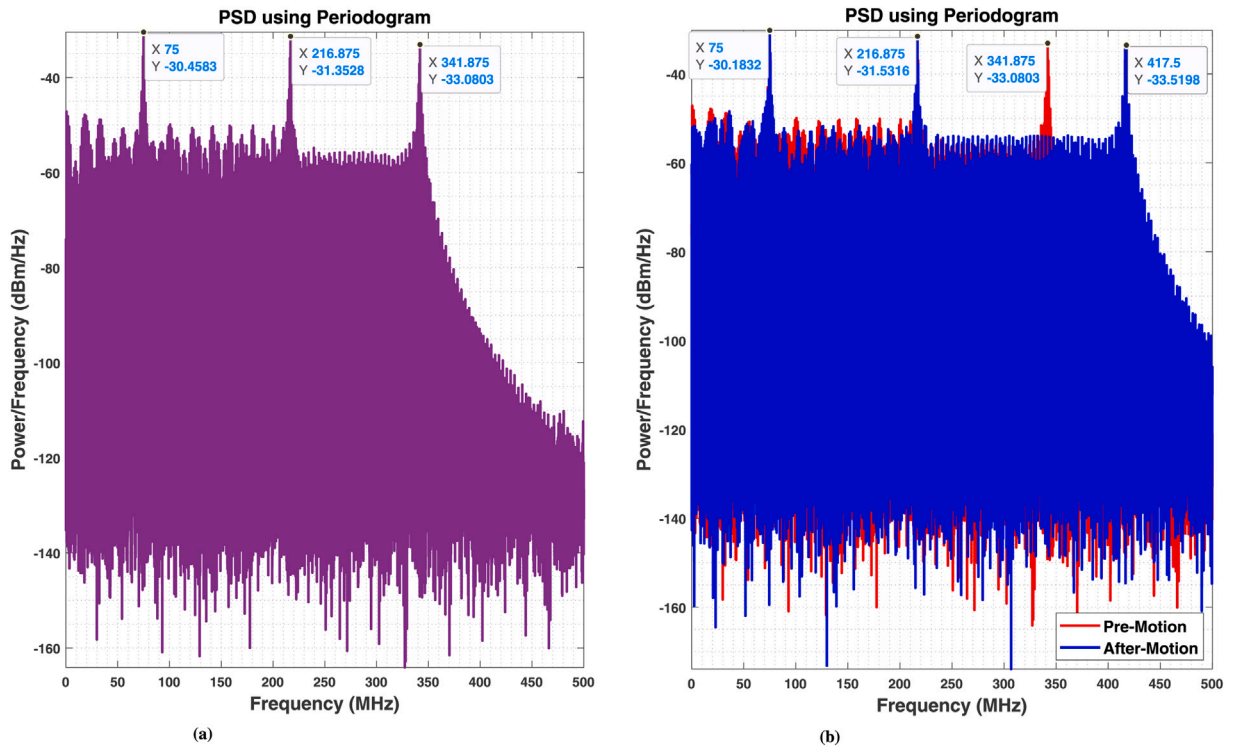
Fig. 8. (a) PSD of LPF dechirped waveform. (b) Pre-motion and after-motion PSD of LPF dechirped waveform. The shift in the PSD 3rd peak from 341.87 MHz to 417.5 MHz due to the change in the 3rd target location from 41 m to 50 m.
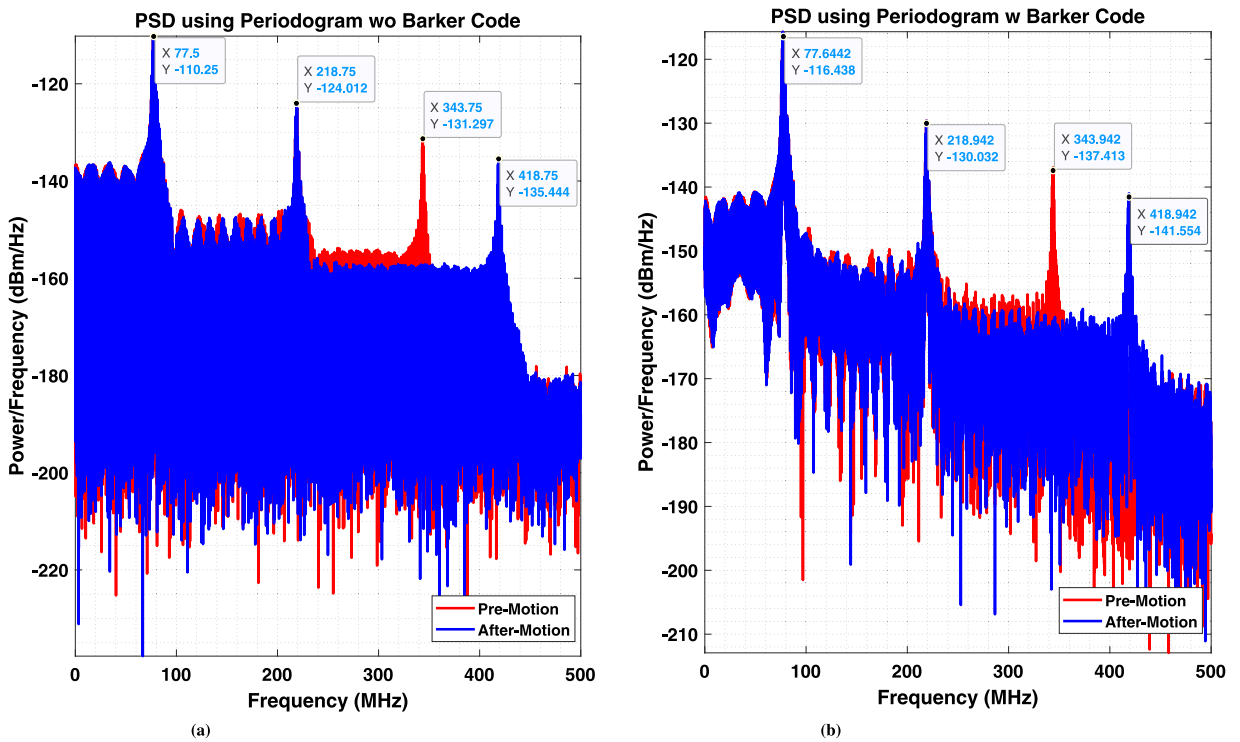

Fig. 9. Pre-motion and after-motion PSD of LPF dechirped waveform (a) Nonideality simulation. (b) Nonideality simulation using barker coded waveform.
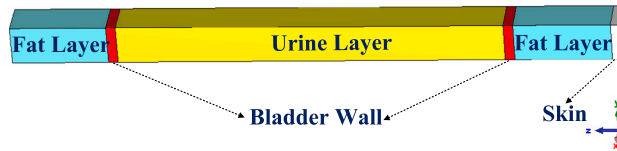
Fig. 10. Multilayer modeling of human abdomen in CST.

Table 3
Dimension and sizes of layers.

Layer name	Dimension and size [cm]
Skin	1.2 × 1.2 × 0.03
Fat	1.2 × 1.2 × 15
Bladder wall	1.2 × 1.2 × 0.3
Urine	1.2 × 1.2 × 3

Table 4
Summary of the location of the peaks in CST simulation.

Urine layer thickness [cm]	1st peak location Δf_1 [MHz]	2nd peak location Δf_2 [MHz]	3rd peak location Δf_3 [MHz]	Δf_1 difference [MHz]
3	84.37	137.502	220.435	–
6	68.75	156.25	243.75	−15.62
9	43.75	184.375	315.626	−25
12	28.12	203.128	384.38	−15.63

Lau, and Gabriel (1996a, 1996b), and then imported into the software. The size and dimensions of each layer are summarized in Table 3. The thickness of the urine layer was incrementally varied from 3 cm to 12 cm, with a step size of 3 cm. Consequently, the thickness of the fat layer was adjusted accordingly to maintain a constant total thickness of the fat and urine layers across each increment of the urine layer thickness during the sweeping process.

The chirp waveform with a 1 GHz bandwidth center frequency of 2.5 GHz with a sweep period ($2 \times T_{sw}$) of 320 ns is used as the transmitted waveform. The waveforms transmitted and reflected from the excitation port are exported to MATLAB for post-data processing. In MATLAB, the transmitted waveform is dechirped using the reflected waveform and then a low-pass filter is applied to it. The spectrum of the LPF dechirped waveform is depicted in Fig. 11. The top left plot in the figure illustrates the simulation result for a urine layer thickness of 3 cm and a fat layer thickness of 12 cm. The top right plot displays the simulation result for a urine layer thickness of 6 cm and a fat layer thickness of 9 cm. The bottom left plot presents the simulation result for a urine layer thickness of 9 cm and a fat layer thickness of 6 cm. Lastly, the bottom right plot showcases the simulation result for a urine layer thickness of 12 cm and a fat layer thickness of 3 cm. Details regarding the location of the first, second, and third peaks, as well as the difference between adjacent first peaks in these plots are summarized in Table 4.

As it is seen, the location of the first peak in the spectrum decreases across the plots, which corresponds to the movement of the anterior bladder wall. As the urine layer thickness increases, the anterior bladder wall moves closer to the excitation port, while the posterior bladder wall moves away from it. Consequently, the delay time for the reflection off the anterior bladder wall decreases, while the delay time for the reflection off the posterior bladder wall increases. The decrease in delay time corresponds to the decrease in the location of the peak in the spectrum of LPF dechirped waveform. The second peak in these plots corresponds to the reflection off the posterior bladder wall, with its location increasing as the urine layer thickness increases. The third reflection occurs off the fat layer at the rear end of the model. The last column of Table 4 shows the difference in first peak location between each urine layer thickness and the next. It was expected that altering the urine layer thickness by a consistent amount would result in an equal shift in the location of the first peak in the spectrum.

6.4. Tissue loss simulation

The depicted model in Fig. 13(a) illustrates the attenuation of EM wave intensity as the wave travels from the transmitting antenna to the receiving antenna. This model corresponds to the one used in Fig. 6. In this analysis, the reflected signal of interest is the reflection off the bladder wall. Therefore, the absorption and reflection from each layer leading up to the bladder wall, as well as the absorption and penetration at the bladder wall, are considered and treated as losses within the multilayer structure. The total path loss is determined by summing the absorption and reflection losses from the initial layer and progressively adding subsequent layers up to the bladder wall layer. This process is mathematically represented in Eq. (21). The same multilayer model used in Section 6.3 is employed for the path loss simulation. The CST simulation is preformed, covering a frequency range of 1 GHz to 10 GHz. Fig. 12(b) presents the loss of each individual tissue across the frequency range, along with the total loss of the entire
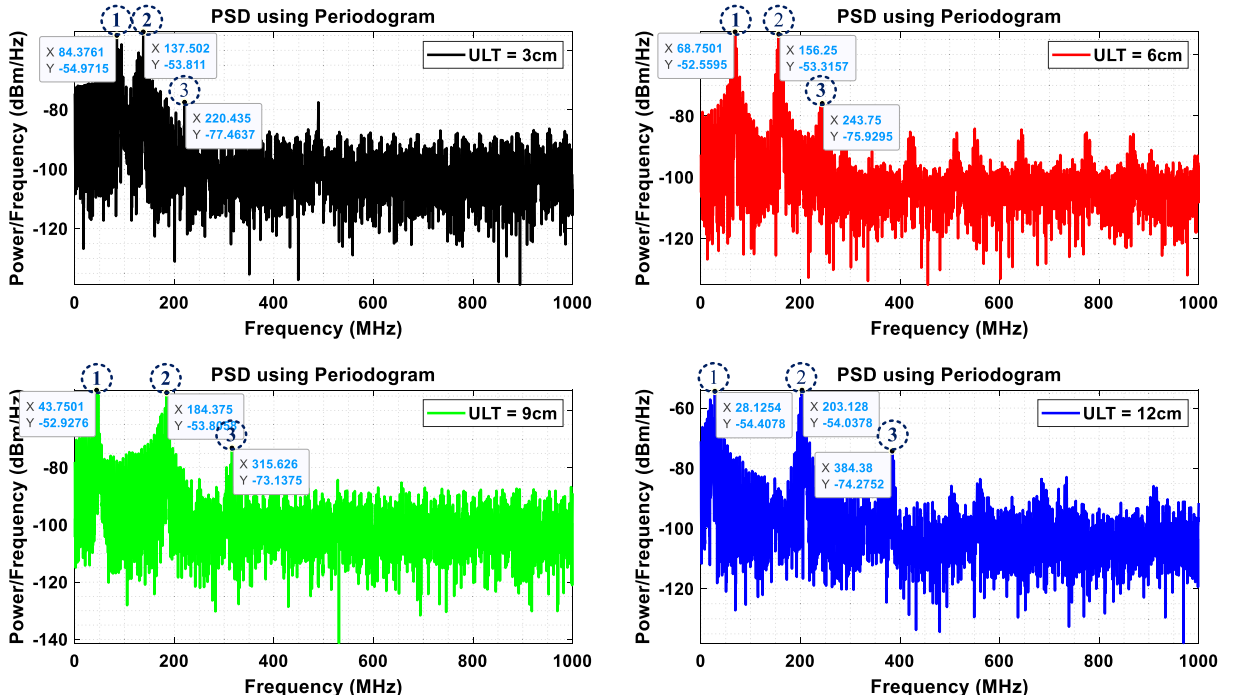
Fig. 11. PSD of LPF dechirped waveform for urine layer thickness of 3, 6, 9 and 12 cm. (1) Anterior bladder wall reflection (2) Posterior bladder wall reflection (3) Posterior fat layer reflection.
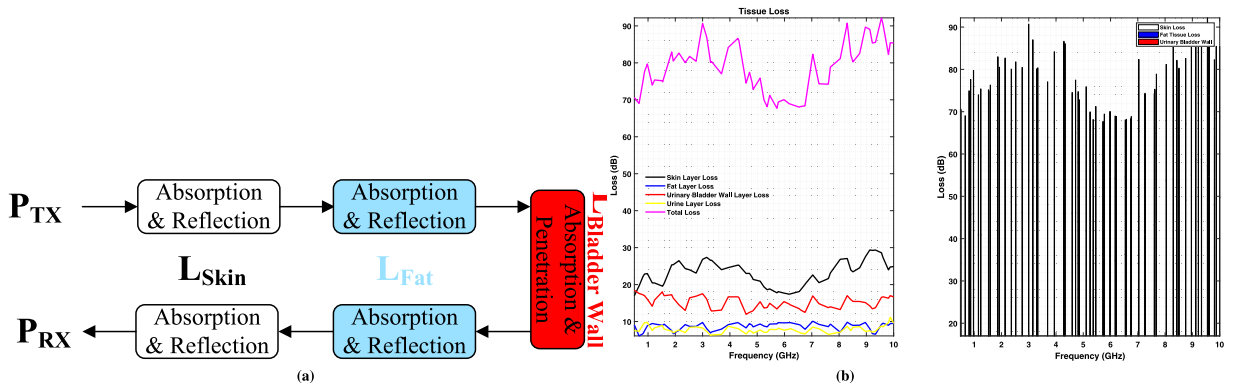

Fig. 12. (a)Model predicting attenuation of EM wave intensity traveling from the transmitting antenna to the receiving antenna. (b) Tissue Loss Simulation in CST.

system displayed in a stacked bar format. Notably, the skin layer exhibits the highest contribution to loss compared to other tissues, while frequencies between 5 GHz and 6 GHz demonstrate the lowest total loss compared to other frequency ranges.

$$L_{total|\text{dB}} = P_{TX|\text{dBm}} - P_{RX|\text{dBm}} = 2 \times L_{Skin|\text{dB}} + 2 \times L_{Fat|\text{dB}} + L_{BladderWall|\text{dB}} \qquad (21)$$

6.5. Measurements in an ex-vivo bladder model

The high-level FMCW radar-based measurement setup for the detection of urine level in the ex-vivo bladder model consists of a vector signal generator (VSG) and a spectrum analyzer (SA) and transmitting and receiving antennas. Fig. 13(a) shows a high-level illustration of the setup, with the exception that the human figure is replaced by the ex-vivo model, described in the following. A R&S SMW unit with 1 GB bandwidth and R&S FSW unit were used as the VSG and SA, respectively, and the antennas were R&S HF907s. In this setup, the chirp is generated by the VSG in the baseband, upconverted to 3 GHz, and amplified to 20 dBm to ensure that the signal reflected off the tissue will have enough power to be detected by the SA. The chirp is then delivered to
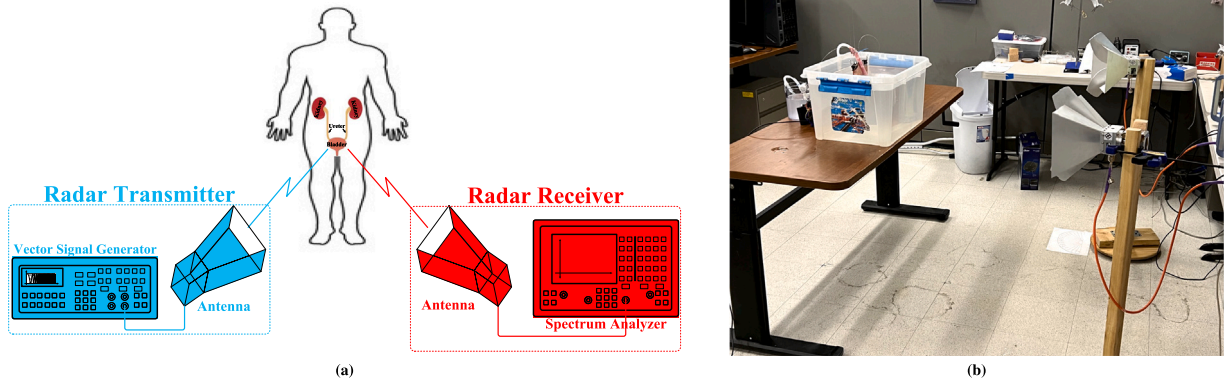
Fig. 13. (a) High-level illustration of FMCW radar-based measurement setup for detection of urine level in Human. (b) Ex-vivo bladder reflection measurement setup; bladder was hung from the ceiling and suspended in plastic tank of water.

the transmit antenna to propagate through the air and toward the model. To address the sensitivity requirements for SA without paying the cost for increased transmission power, a highly directional horn antenna with a focused beam pointed toward the ex-vivo model was used in this measurement. The ex-vivo model consisted of a pig bladder that was filled with 0.9% saline solution in 200 mL increments up to its maximum capacity of 600 mL. 0.9% saline solution was chosen as a filling liquid because of its electrical properties' resemblance to human urine. The solution was added or removed using a digitally-controlled pump designed specifically for this purpose in our lab. The ex-vivo model was developed for proof of concept in which the bladder was hung from the ceiling with thin nylon filament and suspended in a $37 \times 47 \times 28$ cm plastic tank of water. The measurement setup is shown in Fig. 13(b). The antennas were positioned 1 meter apart and the ex-vivo model was centered and positioned 0.5 meter away from each antenna. The antennas were aligned with the ex-vivo model using a laser pointer; the alignment was checked after each change in bladder volume and adjusted if necessary. The EM wave travels from the transmitting antenna through the air and reaches the water in the tank, where the first reflection is generated and picked up by the receiving antenna. The expected location of this peak was around 47.65 MHz, and it was expected to remain at the same location as the bladder volume increased. The next reflections occur from the anterior and posterior bladder walls, respectively, after which the wave is too attenuated to produce detectable reflections. Each of these reflections is distinguishable in time and frequency. However, due to the range resolution of our system, the bladder wall thickness was too thin for the reflections off the anterior and posterior sides of the wall to be detected as separate peaks in the FFT, and they were expected to appear as a single peak. The same holds true for the water tank.

The chirp with I-Q modulation and sweep period $(2 \times T_{sw})$ of 280 ns is used as the transmitted signal. Considering 1 GHz device bandwidth, the chirp rate was 7142.86 MHz/μs. A sampling frequency of $f_s = 2.5$ GHz was selected which is 2.5 times above the baseband chirp bandwidth and above the Nyquist frequency. Coherent integration is used to capture the received I-Q waveform: the received signal is recorded in 12 μs time intervals; when 20 have been recorded they are averaged together to produce the output signal, improving the SNR. Then the solution in the bladder is increased by 200 mL and the data acquisition process is repeated until the maximum capacity of 600 mL is reached. The number of samples during each data acquisition time was $N_s = 30$ k which resulted in a resolution of $f_s/N_s = 83.333$ kHz for the FFT. Assuming that the bladder volume increase for each 200 ml of solution corresponds to 5 cm increase in the location of the bladder anterior wall and considering that the bladder was initially placed in the center of the water tank, the distance from radar to bladder anterior wall was $R_1 = 1.185$ m, $R_2 = 1.235$ m, $R_3 = 1.285$ m and $R_4 = 1.335$ m for $V_1 = 0$ (Empty), $V_2 = 200$ ml, $V_3 = 400$ ml and $V_4 = 600$ ml. Since the EM wave travels through the air into the water, the average propagation speed should be considered while calculating the expected FFT peak locations. The group velocity in lossy medium is given by $v_g = (d\beta/d\omega)^{-1}$, where ω is the angular frequency and β is the imaginary part of the propagation constant, equal to $\gamma(\omega) = j\omega\sqrt{\mu(\epsilon'(\omega) - j\epsilon''(\omega))}$. Knowing the dielectric properties of the tissue and the operating frequency, the group velocity is calculated in each medium. Given the distance of the water tank from the radar ($R_A = 1$ m), the delay time corresponding to water tank reflection was calculated to be $\Delta t_1 = 2 \times R_A/v_A$ where v_A was the propagation speed of the air. Using the same formula for the water media, $\Delta t_2 = 2 \times R_W/v_W$ will result where v_W was considered to be the propagation speed of wave inside the water and R_W is the distance the wave travels inside the water. The average propagation speed of the wave can be calculated by dividing the total distance the wave travels $2 \times (R_A + R_W)$ by the total time delay of $(\Delta t_1 + \Delta t_2)$. Since the distance that the wave travels inside the water is different from one solution increment to the other, the average speed of wave is slightly different in each case. Taking the average propagation speed into account, $\Delta f_2 = 1.051$ GHz, $\Delta f_2 = 1.047$ GHz, $\Delta f_2 = 1.043$ GHz and $\Delta f_2 = 1.039$ GHz is the results for Empty, 200 ml, 400 ml and 600 ml. This information is summarized in Table 5. Fig. 14 shows the measurement results for the first model of ex-vivo measurement. In these plots, the PSD of LPF dechirped waveform for the volume of Empty, 200 ml, 400 ml and 600 ml of bladder solution plotted. As it is seen, the first reflection in all plots happened around 47.65 MHz as expected to be the reflection off the air–water interface. As expected, the location of the second peak in plots decreases as the volume of the solution inside the bladder increases which corresponds to the movement of the bladder wall. As the solution increase, the distance between the antenna and the bladder wall is decreased which results in a decrease in the delay time for the reflection off the bladder wall. The decrease in delay time corresponds to the decrease in the location of the peak in the PSD of LPF dechirped waveform.

Table 5

Summary of the expected location of peaks.

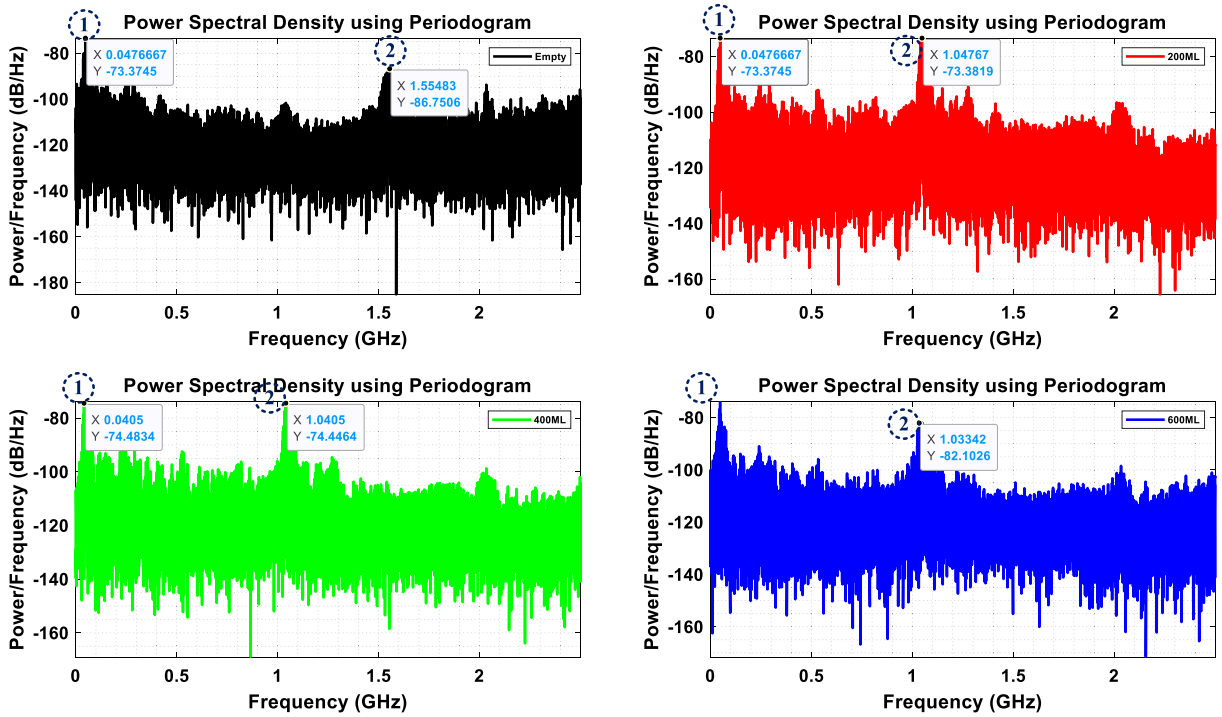| Expected location of peaks				Measured location of peaks		
Volume (ml)	Range (R) [m]	Average propagation speed (V_p)	2nd peak location [GHz]	Δf_2 difference [MHz]	2nd peak location [GHz]	Δf_2 difference [MHz]
$V_2 = 200$	$R_2 = 2.27$	1.54×10^8	$\Delta f_2 = 1.047$	–	$\Delta f_2 = 1.047$	–
$V_3 = 400$	$R_3 = 2.22$	1.55×10^8	$\Delta f_2 = 1.043$	-4	$\Delta f_2 = 1.040$	-7
$V_4 = 600$	$R_4 = 2.17$	1.55×10^8	$\Delta f_2 = 1.039$	-4	$\Delta f_2 = 1.033$	-7

Fig. 14. PSD of LPF dechirped waveform in ex-vivo bladder suspended in the water tank reflection measurement (Top Left) bladder is Empty (Top Right) Bladder is filled 200 ML (Bottom Left) Bladder is filled 400 ML (Bottom Right) bladder is filled with 600 ML. (1) Water tank reflection (2) Anterior bladder wall reflection.

7. Future work

Like any other bladder volume sensing method, the proposed method in a human subject is expected to have other contributors to the measured data other than the contributor of interest, the amount of urine inside the bladder. As a result, using the proposed method for the human subject in the future requires a thorough study of the other contributors to the measurement. In addition, there are several limitations that need to be explored before expecting a fully functional system, some of which are discussed below.

(A) Motion and Patient Posture

The impact of motion and patient posture on the measured data has yet to be explored. In light of this, one idea worth considering is the integration of additional sensors or sensing modalities that can complement our proposed method and capture various aspects of the patient's measurement system. For instance, by incorporating inertial sensors into the wearable device, we can effectively detect the patient's pose, movements, and vibrations. Additionally, it is worth exploring signal processing techniques to identify and eliminate temporary motion-induced peaks. This approach holds significant promise, given that the bladder filling rate is relatively slow compared to human movements. Simple algorithms, such as averaging, can be employed to effectively reject noise caused by motion in the measurements.

(B) Effects of Prolonged Exposure to High-Frequency FMCW

While RF and microwave radiation do not cause ionization of atoms and molecules, prolonged exposure to very high RF intensities can result in the heating of biological tissue and an increase in body temperature. Consequently, tissue damage in humans could occur during exposure to high RF levels because the body may be unable to cope with the excessive heat generated. To mitigate potential risks, the specific absorption rate (SAR) is utilized as a metric to limit the operation of

devices in close proximity to the body, as outlined in the ANSI/IEEE C95.1-1992 guidelines. For instance, the FCC sets a SAR limit of 1.6 W/kg for public exposure from cellular telephones (FCC, 2023). However, considering the slow dynamics of bladder filling, it is not necessary for the patient to continuously monitor their bladder or be constantly aware of its fill state. Therefore, radiation can be significantly reduced via intermittent measurements. The effects of this approach will be explored in the future, after a wearable prototype is built.

Besides what is discussed above, the errors in the measured data can be divided into 2 categories: systematic errors and random errors. An error is considered systematic if it changes in a pattern. For example, this could happen with measurements if, just before the measurements were to be made, something always or often caused the measured data to go up. Since the behavioral pattern of this error is deterministic, the error can be canceled out by subtracting it from the measurement result. The actual system can remove systematic errors by utilizing multiple FMCW radars to take advantage of differential sensing. Random errors in the data can be addressed by capturing the pattern of the patient's bladder voiding and the amount of urine after voiding. Given enough measurement data, the bladder volume estimation algorithm supported by reinforcement learning is expected to cancel out the effect of random error on the measured data which will be addressed in our future work after the complete system is built up.

8. Conclusion

We investigated the feasibility of using an FMCW radar-based method for monitoring urine volume in patients with SCI using an ex-vivo bladder model. A spectral processing algorithm was proposed and investigated through MATLAB simulations to map the urine level to the frequency domain. To verify the proposed spectral processing algorithm and the feasibility of the detection method using FMCW radar, a time domain simulation was performed in CST. Additionally, an ex-vivo measurement was conducted on a porcine bladder filled with saline solution to validate the detection under real conditions. The reflected waveforms were captured and processed to determine the correlation between the amount of frequency shift and the volume increase inside the bladder. The ex-vivo measurement demonstrated promising results for urine level detection in the human bladder using FMCW radar.

CRediT authorship contribution statement

Ata Vafi: Conceptualization, Methodology, Software, Validation, Writing – original draft, Visualization, Investigation. **Conor King:** Writing – review & editing, Software, Visualization, Investigation. **Hanyi Duan:** Visualization, Software, Investigation. **Eric A. Kurzrock:** Methodology, Resources. **Soheil Ghiasi:** Supervision, Writing – review & editing, Funding acquisition, Project administration, Resources.

Declaration of competing interest

The authors declare that they have no known competing financial interests or personal relationships that could have appeared to influence the work reported in this paper.

Data availability

The data that has been used is confidential.

References

Anon (2014). Spinal cord injury facts and figures at a glance. *The Journal of Spinal Cord Medicine*, *37*(4), 479–480.

Coosemans, J., & Puers, R. (2005). An autonomous bladder pressure monitoring system. *Sensors and Actuators A: Physical*, *123–124*(4), 155–161.

Curry, G. Richard (2004). *Radar system performance modeling* (2nd ed.).

Davis, S. K., Van Veen, B. D., Hagness, S. C., & Kelcz, F. (2008). Breast tumor characterization based on ultrawideband microwave backscatter. *IEEE Transactions on Biomedical Engineering*, *55*(1), 237–246.

El-Masri, W., & Fellows, G. (1981). Bladder cancer after spinal cord injury. *Spinal Cord*, *19*(4), 265–270.

EMF-Portal (2023). Accessed: 2023-05-15. https://www.emf-portal.org/en/cms/page/home/effects/radio-frequency.

FCC (2023). Accessed: 2023-05-15. https://www.fcc.gov/engineering-technology/electromagnetic-compatibility-division/radio-frequency-safety/faq/rf-safety.

Fong, D., Alcantar, A. V., Gupta, P., Kurzrock, E. A., & Ghiasi, S. (2018). Non-invasive bladder volume sensing for neurogenic bladder dysfunction management. (pp. 82–85). http://dx.doi.org/10.1109/BSN.2018.8329664.

Fong, D., Yu, X., Mao, J., Saffarpour, M., Gupta, P., Abueshsheikh, R., et al. (2018). Restoring the sense of bladder fullness for spinal cord injury patients. *Smart Health*, *9–10*, 12–22.

Gabriel, S., Lau, R. W., & Gabriel, C. (1996a). The dielectric properties of biological tissues: II. Measurements in the frequency range 10 Hz to 20 GHz. *Physics in Medicine and Biology*, *41*(11), 2251–2269.

Gabriel, S. M., Lau, R., & Gabriel, C. (1996b). The dielectric properties of biological tissues: III. Parametric models for the dielectric spectrum of tissues. *Physics in Medicine and Biology*, *41 11*, 2271–2293.

Gormley, E. A. (2010). Urologic complications of the neurogenic bladder. *The Urologic Clinics of North America*, *37*(4), 601–607.

Hakenberg, O. W., Linne, C., Manseck, A., & Wirth, M. P. (2000). Bladder wall thickness in normal adults and men with mild lower urinary tract symptoms and benign prostatic enlargement. *Neurourology and Urodynamics*, *19*(5), 585–593.

Kurzrock, E. A., & Polse, S. (1998). Renal deterioration in myelodysplastic children: urodynamic evaluation and clinical correlates. *The Journal of Urology*, *159*(5), 1657–1661.

Majerus, S., Basu, A. S., Makovey, I., Wang, P., Zhui, H., Zorman, C., et al. (2016). Wireless bladder pressure monitor for closed-loop bladder neuromodulation. In *Proceedings of IEEE sensors. IEEE international conference on sensors*.

Majerus, S. J., Garverick, S. L., Suster, M. A., Fletter, P. C., & Damaser, M. S. (2012). Wireless, ultra-low-power implantable sensor for chronic bladder pressure monitoring. *ACM Journal on Emerging Technologies in Computing Systems*, *8*(11).

Molavi, B., Shadgan, B., Macnab, A. J., & Dumont, G. A. (2014). Noninvasive optical monitoring of bladder filling to capacity using a wireless near infrared spectroscopy device. *IEEE Transactions on Biomedical Circuits and Systems*, *8*(3), 325–333.

Nahm, L. S., Chen, Y., DeVivo, M. J., & Lloyd, L. K. (2015). Bladder cancer mortality after spinal cord injury over 4 decades. *The Journal of Urology*, *193*(6), 1923–1928.

Schlebusch, T., Nienke, S., Santos, S. A., & Leonhardt, S. (2013). Bladder volume estimation from electrical impedance tomography. 2013, 6441–6444.

Soganci, H., Gezici, S., & Arikan, O. (2009). A Bayesian approach to respiration rate estimation via pulse-based ultra-wideband signals. In *IEEE international conference on ultra-wideband* (pp. 5274–5277).

Stonehill William, H., Dmochowski Roger, R., Patterson Lynn, A., & Cox Claire, E. (1996). Risk factors for bladder tumors in spinal cord injury patients. *The Journal of Urology*, *155*(4), 1248–1250.

Taylor, J. D. (1994). *Introduction to ultra-wideband radar systems* (1st ed.). CRC Press.

Thiel, F., Hein, M., Schwarz, U., Sachs, J., & Seifert, F. (2009). Combining magnetic resonance imaging and ultrawideband radar: A new concept for multimodal biomedical imaging. *Review of Scientific Instruments*, *80*(1), 14–302.

Thorup, J., Biering-Sorensen, F., & Cortes, D. (2012). Urological outcome after myelomeningocele: 20 years of follow-up. *The Journal of Urology*, *188*(3), 890–891.

Vafi, A., Vali, K., Kasap, B., Hu, J. C., Kurzrock, E. A., & Ghiasi, S. (2023). Towards non-invasive bladder volume sensing via bio-impedance spectroscopy: Feasibility demonstration in ex-vivo bladder models. In *ACM/IEEE 14th international conference on cyber-physical systems* (pp. 34–43). New York, NY, USA.

Zito, D., Pepe, D., Mincica, M., Zito, F., De Rossi, D., Lanata, A., et al. (2008). Wearable system-on-a-chip UWB radar for contact-less cardiopulmonary monitoring: present status. In *Annu int conf IEEE eng med biol soc.* (pp. 5274–5277).